Dependence of the Pickup-Like Ion Effective Heating on the Poloidal and Toroidal Magnetic Fields during Magnetic Reconnection

Dependence of the Pickup-Like Ion Effective Heating on the Poloidal and Toroidal Magnetic Fields during Magnetic Reconnection

Shunsuke Usami*

National Institute for Fusion Science,

National Institutes of Natural Sciences, Toki 509-5292, Japan.

The University of Tokyo, Tokyo 113-8654, Japan.

Ritoku Horiuchi and Hiroaki Ohtani

National Institute for Fusion Science,

National Institutes of Natural Sciences, Toki 509-5292, Japan.

SOKENDAI (The Graduate University for Advanced Studies), Toki 509-5292, Japan.

Yasushi Ono, Michiaki Inomoto, and Hiroshi Tanabe

The University of Tokyo, Tokyo 113-8654, Japan.

(Dated: September 14, 2019)

Abstract

The dependence of the ion effective heating on the poloidal (reconnection) and toroidal (guide) magnetic fields during magnetic reconnection in the presence of a guide magnetic field is investigated by means of particle simulations, which mimic merging plasmas in a spherical tokamak (ST). In the previous works, our simulations demonstrated that the ion temperature perpendicular to the magnetic field grows mainly in the downstream, in which ring-shaped velocity distributions are formed. This means that ions are effectively heated. The basic theory explains that the ring-shaped distribution is formed by the ions which rotate around the guide magnetic field while $E \times B$ drifting. In this work, the basic theory is extended to a more general theory including not only a ring-shaped distribution, but also a circular-arc-shaped distribution. The generalized theory explains that the effective temperature changes by the radius and the central angle of the arc-shaped velocity distribution and conjectures the dependence of the ion effective heating on the poloidal and toroidal magnetic fields. The simulations show that the ion heating energy is proportional to the square of the poloidal magnetic field, whereas the ion temperature decreases as the toroidal field is larger, but the toroidal field dependence becomes small for the regime of high toroidal field. These tendencies are consistent with those observed in experiments.

PACS numbers: 52.65.-y, 52.35.Vd, 52.65.Rr, 52.55.Fa

---

*Electronic address: usami.shunsuke@nifs.ac.jp

I.   INTRODUCTION

The merging of spherical tokamaks (STs) attracts attention as a candidate for future fusion reactors because STs can confine higher-β plasmas than standard tokamaks and helical devices [1]. In plasma merging experiments of STs, through magnetic reconnection[2] two torus plasmas with low temperature ($\beta \sim 5\%$) are merged into a single torus plasma with higher temperature ($\beta \sim 40\%$) [3]. It is reported that electrons are heated significantly in the vicinity of the contact point of two torus plasmas, i.e., the X-point of reconnection, while ions are heated dominantly in the downstream, in merging plasmas in STs such as TS-3 and TS-4 at the University of Tokyo [3–6], MRX at the Princeton Plasma Physics Laboratory [7, 8], and MAST at the Culham Centre for Fusion Energy[9, 10].

Comprehension of the heating mechanism during magnetic reconnection can lead to higher-performance for realizing economical ST reactors. As the ion heating mechanism, for example, viscosity heating in shock waves [4, 5], thermalization via remagnetization, collisions, and scattering by wave-particle interactions [8], heating through phase mixing due to the finite Larmor radius effect inside secondary magnetic islands (plasmoids) [11, 12], and heating by kinetic Alfvén waves [13] have been suggested. In the preceding works by Usami *et al.* [14, 15], a new mechanism of the ion heating during magnetic reconnection in the presence of a guide magnetic field has been proposed. The essential point of the mechanism is as follows. Ions behave as nonadiabatic upon crossing the separatrix, and their motion in the downstream is the $E \times B$ drift and the gyromotion. The gyration speed is almost equal to the drift speed and to the reconnection outflow speed, which is much larger than the ion thermal speed in the upstream. Consequently, a ring-shaped ion velocity distribution is formed in the downstream. That is, ions are effectively heated. The radius of the velocity ring, i.e., the gyration speed, corresponds to the effective thermal speed.

In this work, we discuss poloidal (reconnection) and toroidal (guide) field dependence of the ion heating mechanism reported in Refs. [14] and [15] by means of particle simulations and theory. That we use tools of particle simulations is because kinetic physics originating from nongyrotropic motions of electrons and ions, which can not be treated by any models based on the fluid theory, play a predominant role in the magnetic reconnection process including the plasma heating [16].

The paper is organized as follows. In Sec. II, we introduce our particle simulation

model. It is explained that this model mimics the kinetic region covering the contact point of merging plasmas in an ST. In Sec. III, we highlight simulation results and show that ions are effectively heated. Furthermore, we overview the effective heating mechanism as the basic theory. In Sec. IV, we improve the basic theory to construct the generalized theory in order to conjecture the dependence of the ion effective heating on the poloidal and toroidal magnetic fields. In Sec. V, the two types of dependence are confirmed by two series of our particle simulations. Then we compare our simulation results with experimental results in STs, and show that the simulation and experiment results are consistent with each other. Section VI provides a summary of this work.
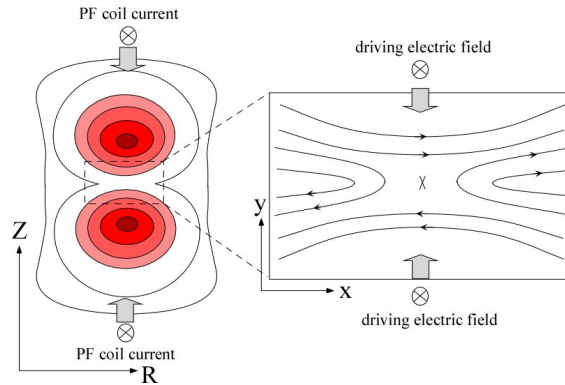
II.   SIMULATION METHOD

FIG. 1: Schematic diagram of our simulation model. The left panel shows merging torus plasmas. The right panel is the area computed by a particle simulation with the PASMO code.

In order to investigate the ion heating mechanism through plasma merging in an ST, we carry out two-dimensional electromagnetic particle simulations. Figure 1 shows a schematic diagram of our simulation model. The left panel shows that two torus plasmas in an ST device are merged. The area surrounded by the dashed line is enlarged in the right panel, which displays the area simulated by our Particle-In-Cell (PIC) code "PASMO" [17–19]. The (R, Z) plane in the ST device corresponds to the (x, y) plane in the simulation. The PIC area covers the kinetic region including the contact point, the X-point.

The simulation model can mimic merging plasmas in an ST because the following two features expressing a plasma merging experiment are implemented in the simulation [20].

4

One is that the guide magnetic field, which corresponds to the toroidal magnetic field in an ST device, is imposed as Horiuchi and Sato applied first [16]. The other is that plasmas are pushed by a driving electric field E_d imposed in the upstream boundary in order to express plasmas pushed by the poloidal field (PF) coil current in an ST. (Hereinafter, we express electric field and magnetic field as E and B, respectively.) The field E_d is set to zero initially and begins to grow first near the center of the upstream. Eventually, E_d develops to reach $E_{dz} = E_0$ in the entire upstream boundary, where E_{dz} is the z-component of E_d. (For detailed information on time evolution of the driving electric field, refer to Ref. [19].) According to Faraday's law, E_d makes the magnetic field at the upstream boundary grow. In particular, from the x-component of Faraday's law, $\partial B_x / \partial t = -c(\partial E_z / \partial y)$, we have that B_x becomes larger as E_{dz} becomes stronger. Thus, by setting different values in E_0, we perform simulations with various strength of the reconnection magnetic field (as shown in Sec. V B). The remaining field quantities at the upstream boundary are set as $E_x = 0$, $\partial E_y / \partial y = 0$. In contrast, the downstream boundary is taken to be free, across which particles can freely go in and out. It is noted that some technical methods are implemented into the PASMO code in order for the particle distribution to be continuous and smooth across the downstream (for detail, see [19]). The following components of the electromagnetic field are taken to be $\partial E_x / \partial x = \partial B_y / \partial x = \partial B_z / \partial x = 0$. The remaining components of the electromagnetic field are derived by solving Maxwell equations at the downstream boundary.

As the initial condition, we take a one-dimensional Harris-type equilibrium with an antiparallel magnetic field in the x direction B_x and a uniform guide magnetic field in the z direction B_z. Thus, we can express the initial state as

$$B_x(y) = B_{x0} \tanh(y/L), \tag{1}$$

$$B_z(y) = B_{z0} \tag{2}$$

$$P(y) = P_0 + B_{x0}^2/(8\pi)\text{sech}^2(y/L) \tag{3}$$

where P represents the plasma pressure. The quantities B_{x0}, B_{z0}, and P_0 are constants, and L is a spatial scale. The initial particle velocity distribution is a shifted Maxwellian distribution, and the temperature is uniform. The initial ion temperature is taken to be equal to the initial electron temperature.

We employ the simulation parameters as follows. The simulation domain size is $(10.54 \times 2.63)c/\omega_{pi}$, where c is the speed of light and ω_{pi} is the ion plasma frequency. The plasma

5

frequency is defined by the use of the initial number density at the neutral line $y = 0$. The initial number of electrons and the initial number of ions are 14,090,240, respectively. The ratio of the electron plasma frequency to the electron gyrofrequency is $\omega_{pe}/\omega_{ce} = 6.0$, where we define $\omega_{ce} = eB_{x0}/(m_e c)$. The Alfvén speed for the total magnetic field $B_0 = \sqrt{B_{x0}^2 + B_{z0}^2}$ is thus expressed as $v_{A0}/c = 0.037$ for the case of $B_{z0} = 2.0 B_{x0}$. The time step is $\omega_{pi}\Delta t = 0.0052$, and the grid spacing is $\Delta_g/(c/\omega_{pi}) = 0.010$.

The simulation domain is relatively small, compared with several studies of magnetic reconnection by the use of particle simulation, for example, in Ref. [21]. In our work, however, we concentrate on ion dynamics responsible for heating in the downstream region not greatly away from the X-point (within $\sim 5d_i$ in simulations). It is also because ion heating occurs in the downstream region not far away from the X-point (but, not in the vicinity of the X-point) in ST devices. Furthermore, we showed in Ref. [15] that the ion temperature profile obtained by the particle simulation was similar to the one in an experimental result in TS-3.

Meanwhile, we confirmed that effects from the downstream boundary did not affect our results, by performing a simulation run under the x-length a little larger than that in the current simulation and comparing them. As a result, we observed that the two kinds of simulation runs demonstrated results almost identical to each other. Moreover, when Ohtani and Horiuchi developed the current version of the PASMO with an open boundary condition, they compared results between a short-sized simulation and a long-sized simulation and confirmed that the results were consistent with each other as shown in Ref. [19].

We use a reduced ion-to-electron mass ratio $m_i/m_e = 100$ to save computer resources. We find no basis for the denying of our effective heating process under condition of the real ion-to-electron mass ratio. It is known that the global structure in the electromagnetic field, which plays an essential role in magnetic reconnection, does not depend on m_i/m_e[22–24]. However, the width of the separatrix δ changes depending on m_i/m_e, because the formation of the separatrix is associated with an electrostatic field originating from the charge separation [25, 26]. Our effective heating mechanism requires the behavior of ions be nonadiabatic across the separatrix. A necessary key condition to the nonadiabatic motion is violation of the magnetic moment conservation and is expressed as $\delta < \rho_i$, which is satisfied in the simulations in this paper, where ρ_i is the ion Larmor radius defined by the use of the magnetic field at the upstream in the vicinity of the separatrix and the thermal speed in the

upstream v_{Ti0}. In 2017, Guo *et al.* estimated that δ is proportional to $(m_i/m_e)^{(1/4)}$ by virtue of particle simulation with the PASMO code [26]. We postulate that the physical quantities with respect to electron do not change with m_i/m_e, which means that m_e is fixed, but only m_i is changed. The ratio of the ion Larmor radius to the electron Larmor radius is expressed as $\rho_i/\rho_e \propto (m_i/m_e)^{(1/2)}$, because the ratio of the ion thermal velocity to the electron thermal velocity is $v_{Ti}/v_{Te} \propto (m_i/m_e)^{(-1/2)}$, assuming that the electron temperature is equal to the ion temperature. It is thus theoretically predicted that $\delta < \rho_i$ is better satisfied as the ion-to-electron mass ratio is larger.

III.   REVIEW OF THE ION EFFECTIVE HEATING
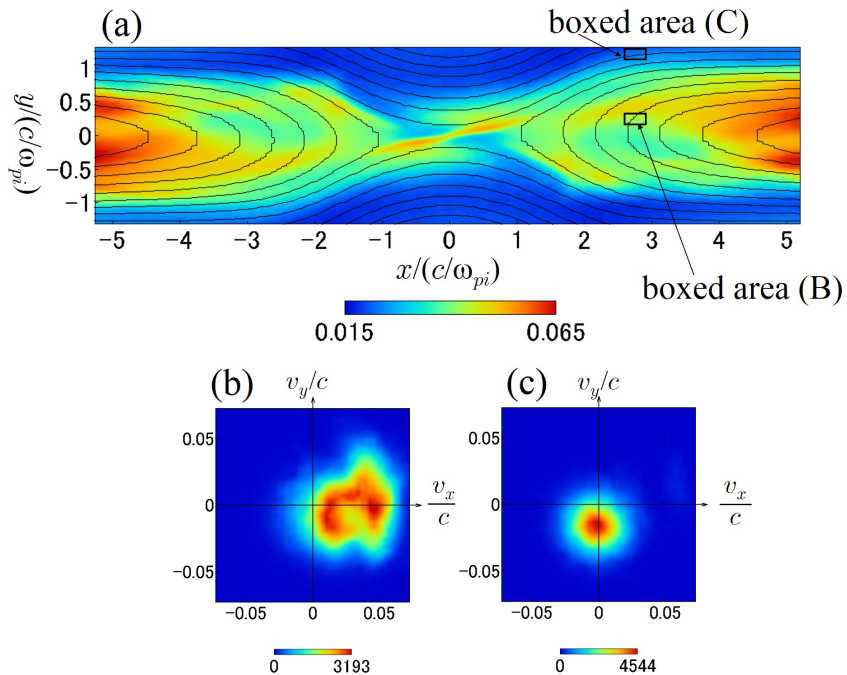
A.   Simulation result

FIG. 2: (a) Spatial profiles of the ion temperature perpendicular to the magnetic field (color contours) and the magnetic field lines at $\omega_{pi}t = 517$. (b) and (c) Ion velocity distributions in the boxed area (B) and (C), respectively. In this simulation run, the reconnection magnetic field is observed to be $B_{\rm rec} = 4.2$.

Let us briefly review the mechanism of the ion effective heating, which has been mentioned

in Refs. [14] and [15]. We display a typical result in the case of $B_g = B_{z0}/B_{x0} = 2$, $L/(c/\omega_{pi}) = 0.66$, and $P_0/(B_{x0}^2/8\pi) = 0.35$ of our particle simulations. Figure 2 (a) shows the spatial profile of magnetic field lines and the ion temperature perpendicular to the local magnetic field $T_{i\perp}$ (color contours) at $\omega_{pi}t = 517$, where the temperature is normalized to $m_e c^2$. Magnetic reconnection is driven by plasmas and magnetic fluxes supplied from the upstream boundary. It is seen that the X-point is located at almost the center of the simulation domain. The reconnection electric field is balanced with $E_0/B_{x0} = -0.04$, i.e., the z-component of the imposed electric field at the upstream. Thus the reconnection system is under a quasi-steady state. The ion temperature rises significantly in the downstream, which is in good agreement with experimental results reported in plasma merging of STs [5, 6]. We show ion velocity distributions at the boxed area (B) in the downstream in Fig. 2 (b) and at the boxed area (C) in the upstream in Fig. 2 (c). In the upstream, it is confirmed that a shifted Maxwellian distribution is fully satisfied. In contrast, it is found that a ring-shaped velocity distribution is formed in the downstream. This indicates that ions are effectively heated in the downstream.

B. Basic theory for the ring-shaped distribution

As the basic theory of the effective heating mechanism, we explain the formation process of the ring-shaped velocity distribution shown in Fig. 2(b) [14, 15]. Now we consider only the global structure of the electromagnetic field in the downstream. That is, it is supposed that the electromagnetic field is uniform and consists of the out-of-plane magnetic field B_z and the convective electric field perpendicular to the magnetic field E_y. In addition, the reconnection outflow speed (in the x direction) is expressed as $u_{\text{out}} = cE_y/B_z$.

First, we observe the motion of ions in the downstream from the Lagrangian point of view. The essential point is that almost all ions enter the downstream from the upstream across the separatrix without passing the X-point, and such ions behave as nonadiabatic upon crossing the separatrix [14, 28, 29]. They are not sufficiently accelerated by the electrostatic field in the separatrix so that their entry speed to the downstream is much less than the reconnection outflow speed u_{out}. We regard the entry speed of the ions as zero. Consequently, the situation to be considered reduces to a simple problem for the ion motion in the downstream. The simple problem is that if initially an ion with zero velocity is placed in the electromagnetic

8

field B_z and E_y, what is the motion of the ion? The solution of this problem is simple. The ion moves in the x direction with the velocity $u_{\rm out} = cE_y/B_z$ owing to the $E \times B(E_y \times B_z)$ drift while gyrating around B_z with speed $u_{\rm out}$. In the velocity space, the ion orbit is drawn as a circle whose center is $(u_{\rm out}, 0)$ and radius is $u_{\rm out}$.
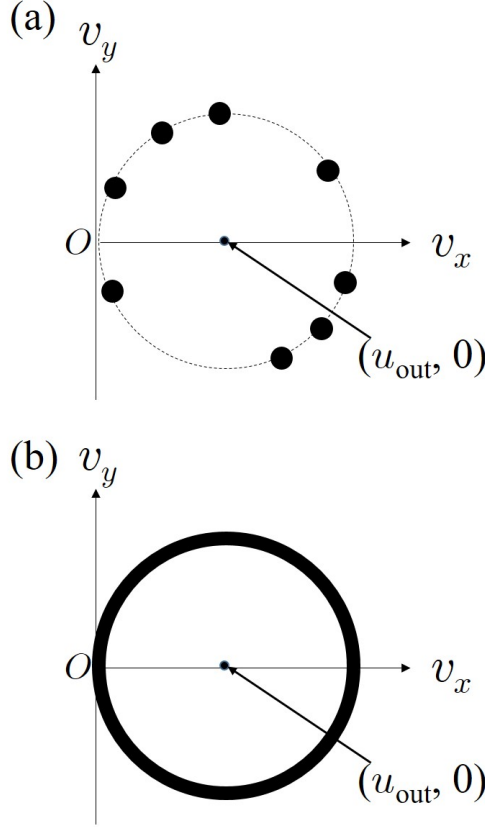

FIG. 3: Formation of ring-shaped velocity distribution. (a) Assuming that the number of ions is small, several ion points are located on the circle. (b) Assuming that the number of ions is very large and the gyromotion phase has no bias, the ion points fill the circle.

Next, let us describe the ion motion from the Eulerian point of view. In the downstream, we focus on a small local area whose size is much smaller than the Larmor radius of the ions with the rotation speed $u_{\rm out}$. As described above, the ions move owing to the $E_y \times B_z$ drift and the gyromotion around B_z in the downstream. However, ions with different gyration phases enter the local area. In the velocity space, at an instant, an ion is plotted as a point assigned on the dotted circle in Fig. 3 (a), where the dotted circle is the trajectory of an ion described from the Lagrangian point of view. Assuming that the number of ions in the

area is very large and the gyration phase of the ions is uniform, the ion points fill the dotted circle as shown in Fig. 3 (b). Consequently, a ring-shaped velocity distribution is formed.

We can obtain the effective temperature of the ring-shaped distribution in the velocity space (v_x, v_y). The effective thermal speed is generally defined as

$$v_{T,j}^2 = \frac{\int (v_j - \langle v_j \rangle)^2 f d^3 v}{\int f d^3 v}, \tag{4}$$

where f is a distribution function, v_j represents the j-component of velocity, and $\langle v_j \rangle$ is the j-component of the averaged velocity. A ring-shaped distribution is two-dimensional and hence the effective temperature is defined as

$$T_{i\perp} = \frac{1}{2} m_i \left(v_{T,x}^2 + v_{T,y}^2 \right), \tag{5}$$

where we express the effective temperature as $T_{i\perp}$, since $v_{T,x}$ and $v_{T,y}$ are perpendicular to the magnetic field. Thus, the effective temperature of the ring-shaped distribution is given as

$$T_{i\perp} = \frac{1}{2} m_i u_{\text{out}}^2. \tag{6}$$

C.   Relation to the "pickup"

In this subsection, we discuss the relationship between the effective heating described in this paper and the "pickup." We clearly classify types of the pickup as the "classical pickup" for particles which are newly ionized in an electromagnetic field and the "novel pickup" for ions not responsible for ionization.

We overview the history of the studies on the picked-up particles. In 1985, Möbius *et al.* proposed the classical pickup, in which a particle which is newly ionized in the solar wind gains kinetic energy from the electromagnetic field of the solar wind [30]. In 1996, Wu *et al.* applied the classical pickup to magnetic reconnection [31, 32]. Wu *et al.* claimed that if hydrogen particles are ionized in the downstream of magnetic reconnection, the newborn protons are accelerated and scattered.

In 2009, Drake *et al.* suggested two cases of the novel pickup applied to magnetic reconnection, which are not related to ionization [27–29], pointing out that when nonadiabatic ions enter the downstream across the separatrix, the ions behave as particles which are freshly ionized in the downstream. First, in Ref. [27], Drake *et al.* investigated the novel

10

pickup in cases of no guide field. Let us name it the "type-I novel pickup." Particle simulations showed that protons are effectively heated on the basis of finding non-Maxwellian velocity distributions indicating counter-streaming. Next, Drake *et al.* addressed the novel pickup in cases of finite guide field, which we call the "type-II novel pickup." In Refs. [28] and [29] it was found that selective heating of heavy ions occurs in the downstream.

Differences between our effective heating process and the type-I and type-II novel pickup are explained. Through the type-I novel pickup, under no guide field, ions gain kinetic energy mainly from the reconnection electric field, while in our effective heating, the ion energy gain is mainly due to in-plane electric field. In addition, the shapes of velocity distribution formed in the downstream are different. A two-belt shape for the type-I novel pickup and a ring (or an arc, which will be shown in this paper) shape for our effective heating process are formed, respectively. Meanwhile, it should be pointed out that our effective heating process is, at first glance, similar to the type-II novel pickup, because the two processes occur in the presence of guide field. However, the following points are different. Only heavy ions as a minor component ion are responsible for the type-II novel pickup. In other words, heavy ions as a minor component ion behave as nonadiabatic and are effectively heated due to the global structure of an electromagnetic field, which is formed by light protons as the main component ion. In contrast, a large percentage of protons as the main component ion are responsible for our effective heating, although protons form the global structure of an electromagnetic field. The difference in heated ion species between our process and the type-II novel pickup is likely to emerge from the difference in the plasma β, and this topic has been discussed in Ref. [14].

IV.   GENERALIZATION OF THE THEORY

In general cases, the velocity distribution is not a complete circle, because the gyromotion phases of the ions inside a local area are not definitely uniform, although the orbit of each ion in the velocity space is drawn as a complete circle, in other words, each ion moves owing to the $E_y \times B_z$ drift and the gyration around B_z. If gyromotion phases of the ions in a local area are limited only within a range, instead of a circle (ring) structure, a circular arc structure of the velocity distribution is formed as a schematic diagram shown in Fig. 4. In the case of an arc-shaped velocity distribution with a central angle α, the ion effective
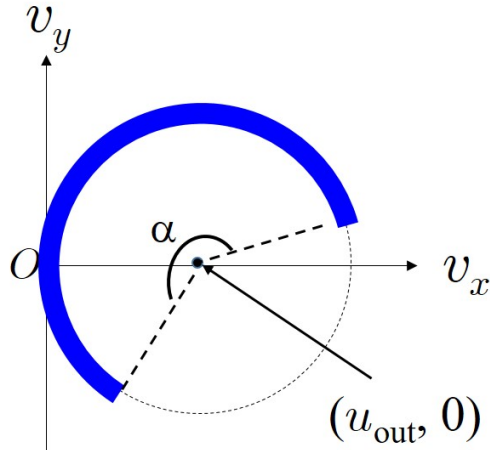
11

FIG. 4: Schematic diagram of circular-arc-shaped velocity distribution with a central angle α. It is noted that the orbit of each ion is a complete circle.

temperature becomes lower than that in a complete circle case. On the basis of the definition Eq. (5), the effective temperature for an arc-shaped velocity distribution is given as

$$T_i = \frac{1}{2} m_i u_{\text{out}}^2 \left[1 - \frac{\sin^2(\alpha/2)}{(\alpha/2)^2} \right]. \tag{7}$$

In the $\alpha = 360°$ case, Eq. (7) is identical to Eq. (6). That is, it can be mentioned that a ring is a specific form of the arcs. Equation (7) can be written as another form,

$$\left[1 - \frac{\sin^2(\alpha/2)}{(\alpha/2)^2} \right] = \frac{2T_i}{m_i u_{\text{out}}^2}. \tag{8}$$

This expression will be used for estimating α for observing the simulation values of the right-hand side in Sec. V C.

As is well known, the reconnection outflow speed u_{out} is nearly equal to Alfvén speed which is defined by use of the reconnection magnetic field B_{rec} and the ion density $n_{i,\text{up}}$ in the upstream [2, 28, 33, 34], that is,

$$u_{\text{out}} \simeq \frac{B_{\text{rec}}}{\sqrt{4\pi m_i n_{i,\text{up}}}}. \tag{9}$$

It is also a reasonable assumption that the ion density in the downstream n_i is proportional to that in the upstream $n_{i,\text{up}}$. Thus, we can arrange Eq. (7) as

$$n_i T_i \propto B_{\text{rec}}^2 \left[1 - \frac{\sin^2(\alpha/2)}{(\alpha/2)^2} \right]. \tag{10}$$

12

Equation (10) theoretically indicates that the ion heating energy is proportional to the square of the reconnection magnetic field, if α is not changed.

Here, let us assume that the circular arc angle α depends on the guide magnetic field B_g, i.e.,

$$\alpha = \alpha(B_g). \tag{11}$$

According to this assumption, we express the ion effective temperature as

$$n_i T_i \propto B_{\text{rec}}^2 \left[1 - \frac{\sin^2(\alpha(B_g)/2)}{(\alpha(B_g)/2)^2} \right]. \tag{12}$$

Equation (12) indicates the dependence of the ion temperature on the reconnection (poloidal) field and on the guide (toroidal) field. (Furthermore, we can theoretically obtain the effective temperature, by taking account of the thickness of an arc-shaped structure. For details, refer to Appendix A.)

We conjecture that α is lower as B_g is larger, but α is larger as B_g is larger in the regime of extremely large B_g. We express a function α as

$$\alpha \propto \frac{1}{B_g^m} + \epsilon B_g^n, \tag{13}$$

where $m > 0$, $n > 0$, and the maximum of α is 2π. We take ϵ to be much less than unity so as to make the second term be dominant for extremely large B_g and be less than the first term for not extremely large B_g. At present, the phrase "extremely large B_g" temporarily means that B_g is larger than ~ 5, because the second term effect is not seen under the condition $B_g \leq 4$, as we show in Sec. V C.

The two types of effects (the first term and the second term in Eq. (13)) are based on theoretical consideration of ion gyromotion phase in the downstream. In Fig. 5, we schematically depict gyromotion of ions and a small local area for observing velocity distribution (a) for small B_g, (b) for large B_g, and (c) for extremely large B_g. The black and red circles indicate the actual positions of ions and the guiding center positions of the ions, respectively, and the dashed lines are gyromotion orbits of the ions. The blue boxes represent the small local areas. The size of the small local areas is fixed throughout Figs. 5 (a)-(c), that is, we enlarge Fig. 5 (c), otherwise gyromotion is too small to be drawn. By virtue of Fig. 5, we discuss the effects of the first term and the second term in Eq. (13) below.

The first effect that α is smaller as B_g is larger is discussed in terms of the guiding center positions of ions. We suppose that in the downstream the ion gyromotion phase depends
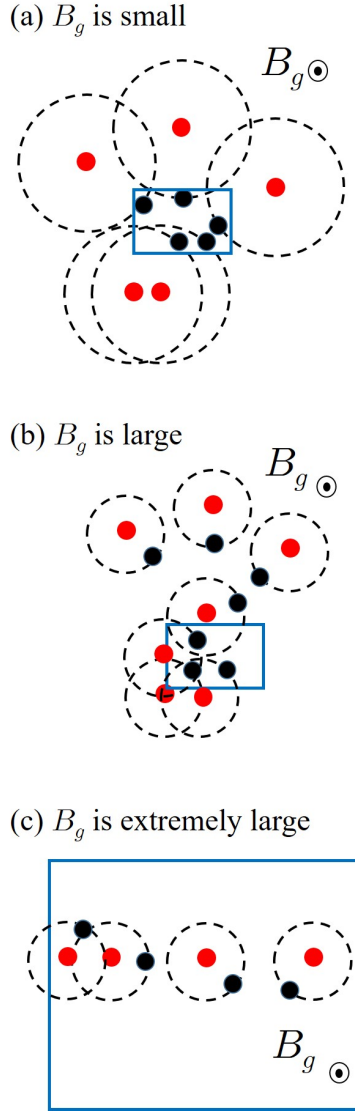
13

FIG. 5: Schematic diagram of ion gyromotion and a small local area for assembling ion particle information to show velocity distribution in the downstream (a) for small B_g, (b) for large B_g, and (c) for extremely large B_g. The black and red circles indicate the actual positions of ions and the guiding center positions of the ions, respectively, and the dashed lines denote gyromotion orbits. The blue boxes represent small local areas.

on the guiding center position. That is, if the guiding center positions of ions are located at an identical position in the downstream, they have the same gyromotion phase. Further, we can extensively presume that if the guiding center positions of ions are close to each other, their gyromotion phases have similar values, while if the guiding center positions of

14

ions are distant from each other, their gyromotion phases have much different values. Now let us observe gyromotion phases of the ions in a small local area as shown in Figs. 5 (a) and (b). Figure 5 (a) shows that in cases in which B_g is small, ions have large Larmor radius. Thereby, the guiding center positions of the ions which exist inside a local area are far away from the local area. According to the above assumption we employed, the ions in the local area have gyromotion phases greatly different from each other. By contrast, Fig. 5 (b) illustrates that in cases of large B_g, ions have small Larmor radius. Hence, the guiding center positions of the ions inside a local area are close to the local area. On the basis of the above assumption, the gyromotion phases of the ions in the local area are not largely different from each other. Let us mathematically express the tendency as $\alpha \propto B_g^{-m}$.

The second effect that the larger B_g is, the larger α is, emerges as the main effect in the regime of extremely large B_g, on the basis of the concept that the size of the local area is small, but is finite. Note that the basic concept always holds, not depending on B_g, and hence the second effect does not disappear, but is only obscured under conditions of small B_g. Figure 5 (c) shows that when B_g is extremely large, the ion Larmor radius is so short that a large part of one gyration orbit begins to fall within the local area. (Eventually, the one gyration orbit will completely fall within the local area.) As a consequence, the gyromotion phases of the ions in a local area cover a wide range. Let us give the tendency as the mathematical expression $\alpha \propto B_g^n$.

Figure 6 (a) depicts an example form of Eq. (13), $\alpha = 8\pi/B_g^2 + (\pi/180)B_g^2$ (we choose $m = n = 2$ and $\epsilon = 1/1440$.) as the solid line. The dashed line indicates the first term $(8\pi/B_g^2)$ and the dotted line represents the second term $((\pi/180)B_g^2)$. In this example, α is monotonically decreased for $B_g < 6$, but the decrease rate becomes less as B_g is larger. For $B_g > 6$, α is monotonically increased. In Fig. 6 (b), we further display $T_{i\perp}$ vs B_g by substituting Eq. (13) into Eq. (12), where $B_{\mathrm{rec}} = n_i = 1$ is set conveniently. It is seen that $T_{i\perp}$ becomes less as B_g is larger, but the decrease rate of $T_{i\perp}$ becomes smaller and rather $T_{i\perp}$ is monotonically increased for $B_g > 7$. Let us, however, emphasize that the graphs in Figs. 6 (a) and (b) should be qualitatively read, but not quantitatively read. By adjusting ϵ in Eq. (13), quantitative behaviors of the dependence of α and thus of $T_{i\perp}$ will be drastically affected. (In this example, we tentatively employ $m = n = 2$ on the basis of somewhat plausible hypothesis, which is, however, developing. Quantitative discussion on Eq. (13) will be performed in the future.)
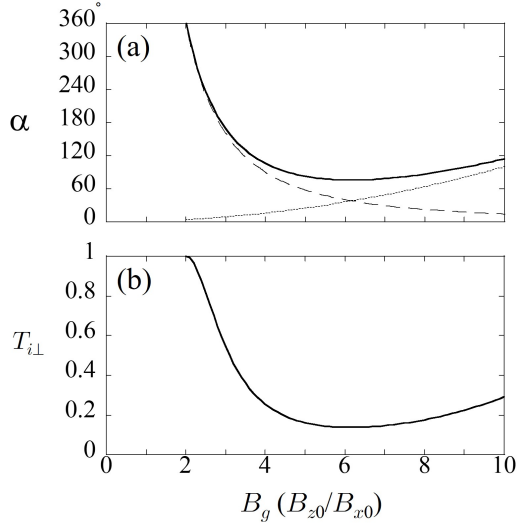
FIG. 6: Examples of $\alpha(B_g)$ and $T_{i\perp}(B_g)$. In the panel (a), the function $\alpha(B_g) = 8\pi/B_g^2 + (\pi/180)B_g^2$ ($\epsilon = 1/1440$) is drawn. In the panel (b), the function $T_{i\perp}(B_g)$ obtained by substituting the above function $\alpha(B_g)$ into Eq. (12) is drawn.
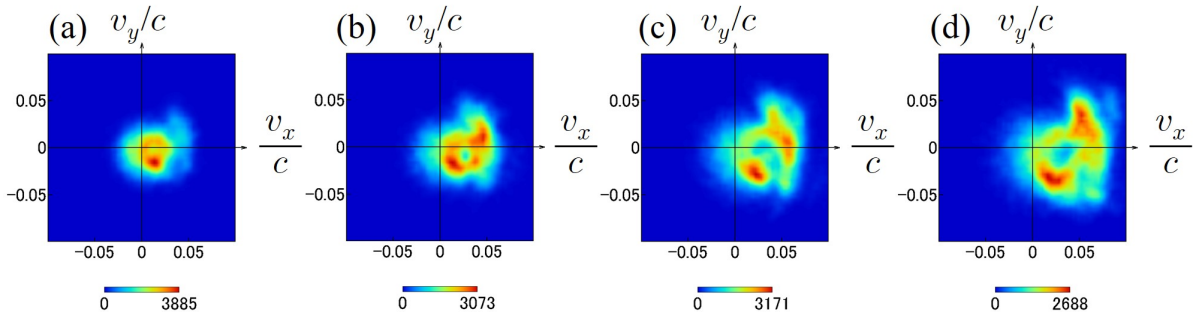

FIG. 7: Ion velocity distributions under various strengths of the reconnection field; (a) $B_{\text{rec}} = 3.0$, (b) 4.2, (c) 5.5, and (d) 6.1. The circle radius of velocity distributions is larger as B_{rec} is larger.

V.   SIMULATION RESULT FOR THE GENERALIZED THEORY

In this section, we demonstrate two series of simulations by using the particle simulation model the same as the one used in Sec. II. Before introducing two series of simulations, we rigidly set up the notation for various quantities, for example, guide magnetic field.
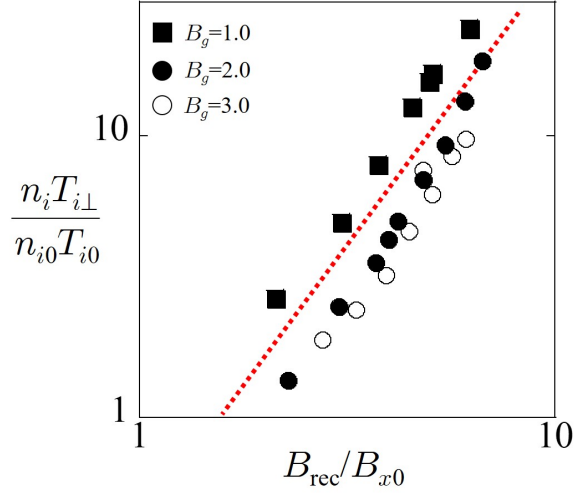
16

FIG. 8: Dependence of the ion heating energy (the ion temperature multiplied by the ion density) on the reconnection magnetic field. The red dotted line represents the theoretical line. Simulation data fit well with the theoretical line.

A.   Notation

In order to avoid confusion for the readers, we clearly define the notation of several quantities. The field B_{x0} and B_{z0} denote the x- and z- components, respectively, of the initial magnetic field in the upstream, and correspond to the reconnection (poloidal) magnetic field and the guide (toroidal) magnetic field in the upstream at the initial state. Let B_g be B_{z0}/B_{x0} in the simulations. In the experiments, B_g corresponds to B_t/B_p, where B_t and B_p are the toroidal and poloidal magnetic fields, respectively. On the other hand, $B_{\rm rec}$ is the reconnection magnetic field at an instant, i.e., the x-component of the magnetic field at an instant, when magnetic reconnection is occurring.

The observed quantities n_i, $T_{i\perp}$, and $u_{\rm out}$ are dependent somewhat on an observation position in the downstream, since the electromagnetic field is not completely uniform in the downstream. Thus, throughout the following results, we use the averaged values over the area of $2.5 < x/(c/\omega_{pi}) < 4.0$ and $-0.3 < y/(c/\omega_{pi}) < 0.3$ as the simulation values of n_i, $T_{i\perp}$, and $u_{\rm out}$. In addition, as the observed value of $B_{\rm rec}$, we use the average value over the upstream boundary lines $(y/(c/\omega_{pi}) = \pm 1.31)$.

The first series of simulations			
Case	B_{rec}	B_g	The range of the local area
(a)	3,0	2.0	$2.30 < (x/(c/\omega_{pi}) < 2.63,\ 0.32 < (y/(c/\omega_{pi}) < 0.49$
(b)	4.2	2.0	$2.30 < (x/(c/\omega_{pi}) < 2.63,\ 0.16 < (y/(c/\omega_{pi}) < 0.32$
(c)	5.5	2.0	$2.63 < (x/(c/\omega_{pi}) < 2.96,\ 0.16 < (y/(c/\omega_{pi}) < 0.32$
(d)	6.1	2.0	$2.96 < (x/(c/\omega_{pi}) < 3.29,\ 0.16 < (y/(c/\omega_{pi}) < 0.32$

TABLE I: Magnetic field components (B_{rec} and B_g) and locations of local areas where velocity distribution is observed for cases (a)-(d) of the first series of simulations. In this series, B_{rec} is changed.

B. Dependence on the reconnection field

As the first series of simulations, let us show the variation of ion velocity distributions by the reconnection magnetic field in Fig. 7. The panels (a), (b), (c), and (d) are typical examples of ion velocity distributions for cases of $B_{\text{rec}} = 3.0$, 4.2, 5.5, and 6.1, respectively, where $B_g = 2.0$. The velocity distributions of the panels (a)-(d) are observed in local areas located at nearly the same position as denoted in Table I. It is clearly seen that as the reconnection field B_{rec} is larger, the circle radius of velocity distribution is larger, that is, the effective temperature is higher.

Figure 8 is a plot of the ion temperature multiplied by the ion density, $n_i T_{i\perp}$, versus the reconnection magnetic field, B_{rec}. Here, $n_i T_{i\perp}$ is normalized to $n_{i0} T_{i0}$, where n_{i0} is the initial ion density at the neutral sheet and T_{i0} is the initial ion temperature. The red dotted line denotes the theoretical line $n_i T_{i\perp} \propto B_{\text{rec}}^2$, predicted by Eq. (12), where note that the proportionality coefficient is chosen as 0.29, but it is not a value obtained from the simulation data. The black squares, black circles, and white circles correspond to simulation data points for the cases of $B_g = 1.0$, 2.0, and 3.0, respectively. We can see that data points fit well with the theoretical line. In addition, we can likely find that data points for each guide field strength fit with the line $n_i T_{i\perp} \propto B_{\text{rec}}^2$ for each proportional coefficient.

Here let us compare the result of Fig. 8 with results in plasma merging experiments in STs, for example, TS-3 in the University of Tokyo. In laboratory experiments, it has been

The second series of simulations			
Case	$B_{\rm rec}$	B_g	The range of the local area
(a)	4,2	2.0	$2.30 < (x/(c/\omega_{pi}) < 2.63, 0.16 < (y/(c/\omega_{pi}) < 0.32$
(b)	4.0	2.5	$2.96 < (x/(c/\omega_{pi}) < 3.29, 0.32 < (y/(c/\omega_{pi}) < 0.49$
(c)	3.9	3.0	$2.63 < (x/(c/\omega_{pi}) < 2.96, 0.32 < (y/(c/\omega_{pi}) < 0.49$
(d)	3.8	4.0	$2.63 < (x/(c/\omega_{pi}) < 2.96, 0.32 < (y/(c/\omega_{pi}) < 0.49$

TABLE II: Magnetic field components ($B_{\rm rec}$ and B_g) and locations of local areas where velocity distribution is observed for cases (a)-(d) of the second series of simulations. In this series, B_g is mainly changed.

reported that the ion heating energy is proportional to the square of the poloidal magnetic field, which is called $B_{\rm rec}^2$-scaling [6, 9]. From this graph, we find that the simulation result is quite consistent with the so-called $B_{\rm rec}^2$-scaling.

C. Dependence on the guide field

Next, we show the second series of simulations, in which the guide magnetic field is changed. Figures 9 (a), (b), (c), and (d) illustrate typical examples of ion velocity distributions for $B_g = 2.0$, 2.5, 3.0, and 4.0, respectively. We use the identical value $E_0/B_{x0} = -0.04$ as the imposed electric field, but we measure slightly different values of $B_{\rm rec}$ for the cases (a)-(d) as shown in Table II. The locations of the local areas for the cases (a)-(d) also are denoted in Table II. Although the dependence on the guide field appears not as clear as the dependence on the reconnection field shown in Fig. 8, we can find a tendency that the angle of arc (or circle) is smaller as the guide magnetic field is larger.

In order to further show the dependence of arc angle on B_g, we estimate the value of α for various cases of B_g by using simulation data. On the basis of the assumption that arc-shaped (containing ring-shaped) velocity distributions are formed, we can obtain α by virtue of Eq. (8), because we can observe $T_{i\perp}$ and $u_{\rm out}$, that is, $2T_{i\perp}/(m_i u_{\rm out}^2)$ in our particle simulation for each B_g case. Figure 10 (a) shows the observed values of $2T_{i\perp}/(m_i u_{\rm out}^2)$ in the simulations. However, it should be noted that the values of $2T_{i\perp}/(m_i u_{\rm out}^2)$ for $B_g < 2$

are greater than 1.0, which can not occur in the framework of the theory for the effective heating mechanism, because it is mathematically clear that the left-hand side of Eq. (8) is less than 1.0. Hence, $2T_{i\perp}/(m_i u_{\mathrm{out}}^2) > 1.0$ means that other thermalization or effective heating processes also play roles in the rise of the ion temperature under the situations of $B_g < 2$. Thus the value of α can not be calculated for the cases of $B_g < 2$. We display a plot of α versus B_g only for $B_g \geq 2$ in Fig. 10 (b). This plot clearly shows the dependence of the arc angle α on the guide field B_g, that is, α is lower as B_g is larger. We can see that the effect of the second term in Eq. (13) (the larger B_g is, the larger α is), which was described in Sec. IV, does not appear, obscured by the effect of the first term, because B_g is not extremely large for all the cases. The second term effect will be investigated in the future.

In this work, we will not discuss the other thermalization or effective heating process which would act for $B_g < 2$, but we simply point out the thickness of an arc or a ring as one candidate for the other processes. If the arc or the ring has a large thickness, the effective temperature is increased as shown in Appendix A.

With respect to the guide field dependence as well, we compare our simulation results with an experimental result in TS-3 [4]. Figure 11 displays a plot of the ion temperature versus the guide magnetic field B_g, where the ion temperature is normalized to the initial temperature. Both the simulation result in Fig. 11 (a) and the experimental result in Fig. 11 (b) show that the ion temperature is lower as the guide (toroidal) magnetic field is larger, but the ion temperature does not change significantly for high B_g regime. (However, the ion temperature becomes almost constant for $B_g > 2$ in Fig. 11 (a) (simulation), while for $B_g > 3$ in Fig. 11 (b) (experiment). This discrepancy might be an important issue for the ion heating. This topic is beyond the current work, and will be discussed in the near future.)

At first glance, we find that there exists an inconsistency between Fig. 9 and Fig. 11 (a). According to Fig. 11 (a), the ion temperature in the case of $B_g = 2.0$ is not very different from that in the case of $B_g = 3.0$, whereas Figs. 9 (a) and (c) demonstrate that the angle ($\alpha \sim 360°$) for $B_g = 2.0$ is greatly different from the angle ($\alpha \sim 180°$) for $B_g = 3.0$. This inconsistency is solved by taking account of the fact that the change in the guide field B_g causes the change in the reconnection field B_{rec} and the ion density n_i as a side-effect which seems to inevitably emerge in simulations for driven magnetic reconnection. Consequently, the outflow speed u_{out} changes with B_g in our particle simulations. It is
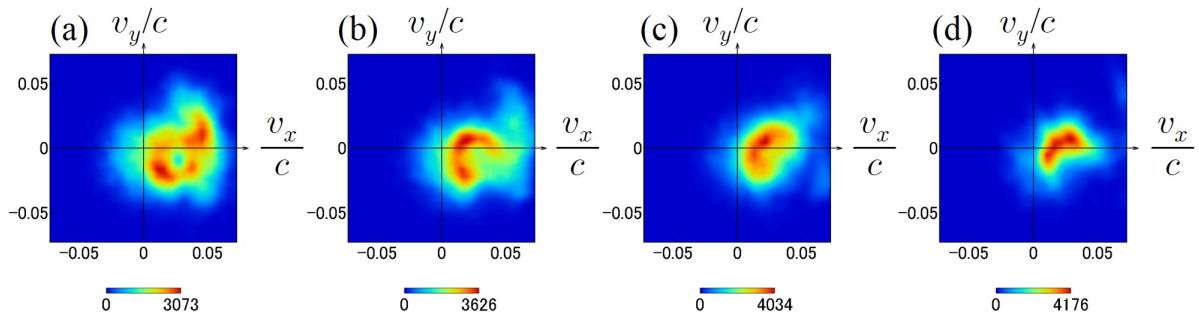
20

FIG. 9: Ion velocity distributions under various strengths of the guide field; (a) $B_g = 2.0$, (b) 2.5, (c) 3.0, and (d) 4.0. The arc angle of velocity distributions is smaller as B_g is larger.

actually observed that u_{out} tends to be larger as B_g is larger, although the driving electric field E_0 is identical. As Eq. (7) indicates, the fast reconnection outflow leads to the rise in the effective temperature. The increment in T_i due to the increase in u_{out} and the decrement in T_i caused by the decrease in α simultaneously play roles in the $B_g = 3.0$ case compared with the $B_g = 2.0$ case so that the ion temperature does not change significantly from the $B_g = 2.0$ case.

VI. SUMMARY

We have investigated the dependence of the ion effective heating on the reconnection and guide magnetic fields by means of particle simulations which mimic plasma merging through magnetic reconnection in an ST device. In our previous work, we found that ions were effectively heated because ring-shaped structures of ion velocity distributions were formed. In addition, we derived a theory of this effective heating. In this work, we have generalized the theory to be applicable for an incomplete ring-shaped, i.e., circular-arc-shaped velocity distribution. The generalized theory explains that the ion effective temperature depends on the radius and the angle of an arc-shaped velocity distribution and conjectures the dependence of the ion heating on the poloidal and toroidal magnetic fields. Our particle simulations have demonstrated the following dependence of the ion heating. (i) The ion heating energy is proportional to the square of the reconnection (poloidal) magnetic field (the B_{rec}^2-scaling). (ii) As the guide (toroidal) magnetic field is stronger, the effective temperature is lower, but this dependence becomes small for high guide field. The two types of dependence (i) and
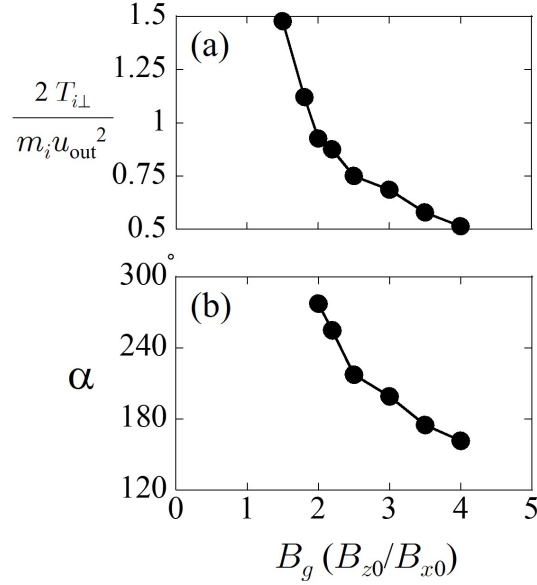
21

FIG. 10: (a) The right-hand side of Eq. (8), $2T_{i\perp}/(m_i u_{out}^2)$ and (b) the arc angle α for different values of the guide field B_g. The angle α tends to be small as B_g is larger. For the regime of $2T_{i\perp}/(m_i u_{out}^2) > 1.0$, the angle α can not be calculated.

(ii) are in good agreement with tendencies reported in experiments.

Acknowledgments

(a) Simulation

$$\frac{T_{i\perp}}{T_{i0}}$$

$B_g \ (B_{z0}/B_{x0})$

(b) Experiment

$$\frac{T_i}{T_{i0}}$$
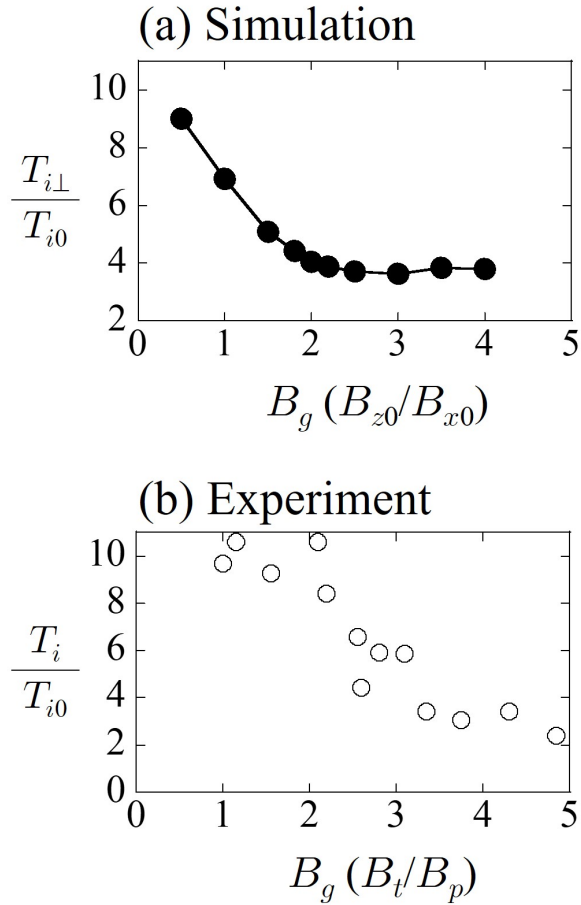
$B_g \ (B_t/B_p)$

FIG. 11: Dependence of the ion temperature on the guide magnetic field. The panels (a) and (b) plot results obtained by our simulations and reported in TS-3 experiments. respectively. The tendencies seen in the panels (a) and (b) are in good agreement with each other.

Appendix A: Finite thickness of an arc-shaped velocity distribution

Let us calculate the effective temperature for the case that an arc-shaped velocity distribution has a finite thickness as shown in Fig. 12.

In Fig. 12 (a), an arc-shaped velocity structure has a thickness V in the direction of the arc center $(u_{\text{out}}, 0)$. We divide the situation of Fig. 12(a) into two cases, which differ in density distribution. In one case, we assume that the particle density is completely uniform inside the arc structure with a thickness (the light blue region). We theoretically obtain the
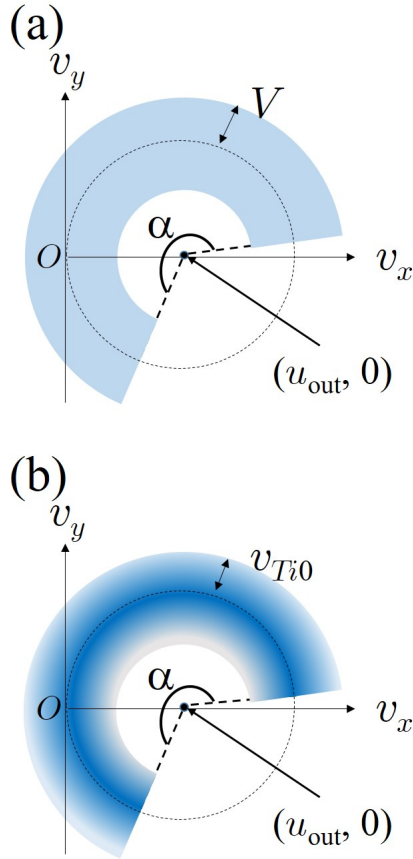
23

FIG. 12: Schematic diagram of an arc-shaped structure with a finite thickness in the arc center direction. In the panel (a), an arc has a thickness V, in which the particle density is uniform for one case, and in which the particle density is inversely proportional to the distance from the arc center for the other case, i.e., $\propto 1/v_{\perp 1}$, where $v_{\perp 1}$ is a velocity component in the arc center direction. In the panel (b), an arc has a thickness, in which the particle density is a function of the distance from the arc center. Here the function is assumed to be $\propto (1/v_{\perp 1})f_G(v_{\perp 1})$, where f_G is a Gaussian function whose width is $v_{\mathrm{Ti}0}$ and whose center is the dotted line.

effective temperature in the case as follows,

$$T_i = \frac{1}{2}m_i \left[(u_{\mathrm{out}}^2 + V^2)\left\{ 1 - \frac{\sin^2(\alpha/2)}{(\alpha/2)^2} \right\} + \frac{1}{9}V^2 \left\{ 3 - \frac{V^2}{u_{\mathrm{out}}^2} \right\} \frac{\sin^2(\alpha/2)}{(\alpha/2)^2} \right]. \tag{A1}$$

As the other case in Fig. 12 (a), we discuss the situation that an equal number of particles exist on any concentric arc line $(v_x - u_{\mathrm{out}})^2 + v_y^2 = (u_{\mathrm{out}} + V_a)^2$, not depending on V_a $(-V < V_a < V)$. Thus, the density function is given as $\propto 1/v_{\perp 1}$, where $v_{\perp 1}$ denotes

a velocity component in the arc center direction. In this case, the particle density is not completely uniform; the density is slightly higher in inner region of the arc, and the density is slightly lower in the outer region. This density distribution is plausible if we consider that ions continuously enter the downstream, with uniform distribution of v_{x0}, the x-component of entry velocity, within the range from $-V$ to V. (The y-component of entry velocity is assumed to be zero for all the ions.) Their gyroperiod is the same, not depending on the entry velocity, while the orbit length depends on v_{x0}; the smaller v_{x0}, shorter the orbit length. Therefore, we are allowed to assume that the number of particles is equal on any concentric arc line. The effective temperature in the case is obtained as

$$T_i = \frac{1}{2} m_i \left[u_{\text{out}}^2 \left\{ 1 - \frac{\sin^2(\alpha/2)}{(\alpha/2)^2} \right\} + \frac{1}{3} V^2 \right]. \tag{A2}$$

Next, we employ a different type of arc thickness. In Fig. 12 (b) as well, an arc-shaped velocity structure has a thickness in the center direction. The color gradation means that in the arc center direction, the particle density satisfies a Gaussian function f_G with the standard deviation v_{Ti0} (the initial thermal velocity) and with the mean value expressed as the dotted line $(v_x - u_{\text{out}})^2 + v_y^2 = u_{\text{out}}^2$. Thus, the density function is given as $\propto (1/v_{\perp1}) f_G(v_{\perp1})$. That is, let us suppose that particle velocities in the arc center direction satisfy a Maxwellian. (The same condition in the latter case of Fig. 12 (a) holds for the case of Fig. 12 (b). We consider that ions continuously enter the downstream, with Gaussian distribution of v_{x0}, x-component of entry velocity. Hence, the density at an inner position is higher than that at an outer position, where the inner position and the outer position have an equal distance from the dotted line.) This assumption is likely to be appropriate, because ions are regarded to gain almost no kinetic energy upon crossing the separatrix, and thus each ion enters the downstream with keeping each initial velocity. Then in the downstream, each ion has each constant gyration speed, and their $E \times B$ drift velocities are identical to $(u_{\text{out}}, 0)$, under the assumption of uniform electromagnetic field in the downstream. Actually, we can see that a ring-shaped velocity distribution shown in Fig. 2 (b) has a thickness, which is nearly equal to v_{Ti0}, comparing the velocity distribution shown in Fig. 2 (c), which is a Maxwellian distribution with the thermal speed v_{Ti0}. Thus, the effective ion temperature is

given as

$$
\begin{aligned}
T_i &= \frac{1}{2}m_i \left[u_{\text{out}}^2 \left\{ 1 - \frac{\sin^2(\alpha/2)}{(\alpha/2)^2} \right\} + v_{Ti0}^2 \right] \\
&= \frac{1}{2}m_i u_{\text{out}}^2 \left\{ 1 - \frac{\sin^2(\alpha/2)}{(\alpha/2)^2} \right\} + \frac{1}{2}T_{i0}.
\end{aligned} \tag{A3}
$$

Note that Eq. (A3) is not applicable although it is arithmetically correct, if α is infinitesimal. Also, in Eq. (A3), it will be of interest that the half of the initial (real) temperature is added into the effective temperature after heating. The reasons for these two points are related to each other.

When α is quite close to zero, Eq. (A3) is nearly equal to $(1/2)T_{i0}$. This result is quite startling, if we consider the following situation. If the electromagnetic field in the separatrix and in the downstream were equal to that in the upstream (although this situation is impossible), obviously the pickup-like process would not work, and hence α should be zero. Thus, Eq. (A3) leads to one result that the ion temperature is $(1/2)T_{i0}$ as shown above. On the other hand, the ion velocity distribution must maintain the initial Maxwellian distribution, because we regard that the electromagnetic field is constant throughout the whole region. Thereby, we obtain a different result that the ion temperature is T_{i0}. This discrepancy indicates that Eq. (A3) is not applicable to infinitesimal α.

The inconsistency is originated from the following logic. When we derive Eq. (A3), we take into account only a thermal velocity component in the direction of the arc center $v_{Ti0,1}$, and we inevitably ignore a thermal velocity component in the tangential direction $v_{Ti0,2}$, where $v_{Ti0,1} = v_{Ti0,2} = v_{Ti0}$ is assumed. The component $v_{Ti0,2}$ causes the arc to spread in the tangential direction, but the spreading due to $v_{Ti0,2}$ is necessarily masked by the tangential width α of the arc itself. The emergence of $(1/2)T_{i0}$ in Eq. (A3) is based on the fact that $v_{Ti0,1}$ is contained in the derivation process of Eq. (A3), but $v_{Ti0,2}$ can not be contained. Nevertheless, if α is infinitesimal, tangential spreading due to $v_{Ti0,2}$ is not masked by the tangential width α of the arc itself. Hence, Eq. (A3) does not hold for a case that α is infinitesimal, i.e., roughly estimating, $\alpha u_{\text{out}} < v_{Ti0}$.

---

[1] M. Gryaznevich, R. Akers, P. G. Carolan, N. J. Conway, D. Gates, A. R. Field, T. C. Hender, I. Jenkins, R. Martin, M. P. S. Nightingale, C. Ribeiro, D. C. Robinson, A. Sykes, M.

Tournianski, M. Valovič, and M. J. Walsh, Phys. Rev. Lett. **80**, 3972 (1998).

[2] M. Yamada, Phys. Plasmas **14**, 058102 (2007).

[3] Y. Ono, T. Kimura, E. Kawamori, Y. Murata, S. Miyazaki, Y. Ueda, M. Inomoto, A. L. Balandin, and M. Katsurai, Nucl. Fusion **43**, 789-794 (2003).

[4] Y. Ono, Y. Hayashi, T. Ii, H. Tanabe, S. Ito, A. Kuwahata, T. Ito, Y. Kamio, T. Yamada, M. Inomoto, and TS-Group, Phys. Plasma **18**, 111213 (2011).

[5] Y. Ono, H. Tanabe, Y. Hayashi, T. Ii, Y. Narushima, T. Yamada, M. Inomoto, and C. Z. Cheng, Phys. Rev. Lett. **107**, 185001 (2011).

[6] Y. Ono, H. Tanabe, T. Yamada, M. Inomoto, T. Ii, S. Inoue, K. Gi, T. Watanabe, M. Gryaznevich, R. Scannell, C. Michael, and C. Z. Cheng, Plasma Phys. Control. Fusion **54**, 124039 (2012).

[7] M. Yamada, J. Yoo, J. Jara-Almonte, H. Ji, R. M. Kulsrud, and C. E. Myers, Nature Communications **5**, 4774 (2014).

[8] J. Yoo, M. Yamada, H. Ji, J. Jara-Almonte, and C. E. Myers, Phys. Plasmas **21**, 055706 (2014).

[9] H. Tanabe, T. Yamada, T. Watanabe, K. Gi, M. Inomoto, R. Imazawa, M. Gryaznevich, R. Scannell, N. J. Conway, C. Michael, B. Crowley, I. Fitzgerald, A. Meakins, N. Hawkes, K. G. McClements, J. Harrison, T. O'Gorman, C. Z. Cheng, Y. Ono, and The MAST Team, Nucl. Fusion **57**, 056037 (2017).

[10] H. Tanabe, T. Yamada, T. Watanabe, K. Gi, M. Inomoto, R. Imazawa, M. Gryaznevich, C. Michael, B. Crowley, N. J. Conway, R. Scannell, J. Harrison, I. Fitzgerald, A. Meakins, N. Hawkes, K. G. McClements, T. O'Gorman, C. Z. Cheng, Y. Ono, and MAST Team, Phys. Plasmas **24**, 056108 (2017).

[11] N. F. Loureiro, A. A. Schekochihin, and A. Zocco, Phys. Rev. Lett. **111**, 025002 (2013).

[12] R. Numata and N. F. Loureiro, J. Plasma Phys. **81**, 305810201 (2014).

[13] J. Liang, Y. Lin, J. R. Johnson, Z. X. Wang, and X. Wang, Phys. Plasmas **24**, 102110 (2017).

[14] S. Usami, R. Horiuchi, and H. Ohtani, Phys. Plasmas **24**, 092101 (2017).

[15] S. Usami, R. Horiuchi, H. Ohtani, Y. Ono, and H. Tanabe, Plasma Fusion Res. **13**, 3401025 (2018).

[16] R. Horiuchi and T. Sato, Phys. Plasmas **4**, 277 (1997).

[17] W. Pei, R. Horiuchi, and T. Sato, Phys. Rev. Lett. **87**, 235003 (2001).

[18] W. Pei, R. Horiuchi, and T. Sato, Phys. Plasmas **8**, 3251 (2001).

[19] H. Ohtani and R.Horiuchi, Plasma Fusion Res. **4**, 024 (2009).

[20] S. Inoue, Y. Ono, H. Tanabe, R. Horiuchi, and C. Z. Cheng, Nucl. Fusion **55**, 083014 (2015).

[21] K. Fujimoto, Front. Phys. **6**, 119 (2018).

[22] R. Horiuchi and T. Sato, Phys. Plasmas **1**, 3587-3597 (1994).

[23] P. Ricci, G. Lapenta, and J. U. Brackbill, Geophys. Res. Lett. **29**, 2088 (2002).

[24] P. L. Pritchett, J. Geophys. Res. **115**, A10208 (2010).

[25] C. Z. Cheng, S. Inoue, Y. Ono, and R. Horiuchi, Phys. Plasmas **22**, 101205 (2015).

[26] X. Guo, R. Horiuchi, C. Z. Cheng, T. Kaminou, and Y. Ono, Phys. Plasmas **24**, 032901 (2017).

[27] J. F. Drake, M. Swisdak, T. D. Phan, P. A. Cassak, M. A. Shay, S. T. Lepri, R. P. Lin, E. Quataert, and T. H. Zurbuchen, J. Geophys. Res. **114**, A05111 (2009).

[28] J. F. Drake, P. A. Cassak, M. A. Shay, M. Swisdak, and E. Quataert, Astrophys. J. **700**, L16 (2009).

[29] J. F. Drake and M. Swisdak, Phys. Plasmas **21**, 072903 (2014).

[30] E. Möbius, D. Hovestadt, B. Klecker, M. Scholer, G. Gloeckler, and F. M. Ipavich, Nature **318**, 426 (1985).

[31] C. S. Wu, Astrophys. J. **472**, 818-826 (1996).

[32] C. S. Wu, Y. Li, J. K. Chao, P. H. Yoon, and L. C. Lee, Astrophys. J. **495**, 951-956 (1998).

[33] M. A. Shay, J. F. Drake, B. N. Rogers, R. E. Denton, J. Geophys. Res. **106**, 3759-3772 (2001).

[34] T. Sato and T. Hayashi, Phys. Fluids **22**, 1189-1202 (1979).